PHYSICAL REVIEW B **90**, 075203 (2014)

Band gap renormalization and Burstein-Moss effect in silicon- and germanium-doped wurtzite GaN up to 10^{20} cm^{-3}

Martin Feneberg,[*] Sarah Osterburg, Karsten Lange, Christian Lidig, Bernd Garke, and Rüdiger Goldhahn
Institut für Experimentelle Physik, Otto-von-Guericke-Universität Magdeburg, Universitätsplatz 2, 39106 Magdeburg, Germany

Eberhard Richter and Carsten Netzel
Ferdinand-Braun-Institut, Leibniz-Institut für Höchstfrequenztechnik, Gustav-Kirchhoff-Straße 4, 12489 Berlin, Germany

Maciej D. Neumann and Norbert Esser
Leibniz-Institut für Analytische Wissenschaften - ISAS - e.V., Albert-Einstein-Straße 9, 12489 Berlin, Germany

Stephanie Fritze, Hartmut Witte, Jürgen Bläsing, Armin Dadgar, and Alois Krost
Institut für Experimentelle Physik, Otto-von-Guericke-Universität Magdeburg, Universitätsplatz 2, 39106 Magdeburg, Germany
(Received 28 February 2014; revised manuscript received 31 July 2014; published 18 August 2014)

The interplay between band gap renormalization and band filling (Burstein-Moss effect) in n-type wurtzite GaN is investigated. For a wide range of electron concentrations up to 1.6×10^{20} cm^{-3} spectroscopic ellipsometry and photoluminescence were used to determine the dependence of the band gap energy and the Fermi edge on electron density. The band gap renormalization is the dominating effect up to an electron density of about 9×10^{18} cm^{-3}; at higher values the Burstein-Moss effect is stronger. Exciton screening, the Mott transition, and formation of Mahan excitons are discussed. A quantitative understanding of the near gap transition energies on electron density is obtained. Higher energy features in the dielectric functions up to 10 eV are not influenced by band gap renormalization.

DOI: 10.1103/PhysRevB.90.075203 PACS number(s): 78.20.Ci, 71.35.−y, 71.45.Gm

I. INTRODUCTION

Layers exhibiting high carrier densities are the basis of any electrically driven semiconductor device in electronics or optoelectronics. The wide band gap semiconductor GaN has gained importance as a material basis for both types of devices. As examples, we only name nitride high-electron mobility transistors and blue light emitting or laser diodes. Despite the successful application of GaN, the fundamental understanding of basic physical properties induced by high electron concentrations is still insufficient.

In this paper we discuss one of the most important semiconductor material parameters, namely the fundamental band gap and related transition energies as a function of free electron concentration due to doping. It has been well known for decades that an increase in carrier density leads to filling of states in the band, thus shifting the absorption onset to higher energies. This effect was independently found by Moss [1] and Burstein [2] in 1954 and is called Burstein-Moss shift (BMS). It is strongest in narrow band gap semiconductor materials because the effective mass increases with increasing band gap roughly as $m^*/m_0 \propto E_G/20\,\text{eV}$, and the density of states $D(E)$ is proportional to $m^{*3/2}$ in three-dimensional material. A larger band gap thus leads to a larger density of states which is only filled for higher electron concentrations, which are on the other hand harder to achieve for larger band gap materials.

In contrast, band gap renormalization (BGR) [3] decreases the fundamental band gap energy E_G with increasing carrier density due to electron-electron and electron-ion interaction. Because both BGR and BMS affect the semiconductor simultaneously, the absorption onset is found by superposition of both energy shifts. In a certain carrier density regime BGR and BMS have very similar magnitude, yielding a nearly constant absorption onset which is discussed in detail below.

For lower band gap semiconductors, these effects were identified and discussed decades ago. An excellent early review is provided by Ref. [4]. Few years later, Mahan discussed from theoretical point of view the different participating energy terms in renormalization vs Burstein-Moss shift [5]. His results still hold today; he, however, treated the more complicated case of the indirect semiconductors Si and Ge having several equivalent conduction bands.

BGR and BMS are of major importance for understanding GaN already within technically relevant electron doping ranges. Surprisingly enough, only little attention was paid to BMS and BGR in GaN. The BMS in GaN was observed already in 1994 [6] but then only scarcely investigated later [7]. Recently this subject is moving back to the focus of scientific research [8] partly due to the success of germanium doping up to electron concentrations of 10^{20} cm^{-3} [9,10]. For BGR in GaN there are earlier studies investigating the renormalization effects due to intense optical excitation [11–13], but only little work is done on BGR due to unipolar doping [14–18] which of course concerns the BMS as well.

Due to great improvements in sample quality mirrored by the increasing availability of GaN pseudo-substrates, substrates [19], and, e.g., the high-electron density doping of GaN by germanium [9,10] we extend the current knowledge to a quantitative understanding of the interplay between BMS and BGR in wurtzite GaN which has not been achieved so far. Earlier studies relied on empirical descriptions of BGR

---

[*] Corresponding author: martin.feneberg@ovgu.de

TABLE I. Summary of samples and collection of lattice parameters, electron concentration as determined by Hall effect measurements and infrared ellipsometry, and secondary ion mass spectroscopy data where available.

Sample	Growth method	Dopant	n_{Hall} (cm^{-3})	n_{IRSE} (cm^{-3})	[Si,Ge] (cm^{-3})	μ_{Hall} ($\mathrm{cm}^2/\mathrm{Vs}$)	a (Å)	c (Å)
A	HVPE		1.4×10^{12}			368	3.1892	5.1854
B	HVPE	Si	8.7×10^{17}		1×10^{18}	400	3.1887	5.1856
C	HVPE	Si	1.8×10^{18}	1.5×10^{18}	2×10^{18}	320	3.1898	5.1854
D	HVPE	Si	3.3×10^{18}	3.8×10^{18}	4×10^{18}	260	3.1892	5.1854
E	HVPE	Si	7.3×10^{18}	6.5×10^{18}	8×10^{18}	220	3.1889	5.1855
F	HVPE	Si	1.4×10^{19}	1.4×10^{19}	1.6×10^{19}	204	3.1890	5.1855
G	MOCVD	Ge	3.4×10^{19}	3.9×10^{19}		125	3.1835	5.1892
H	MOCVD	Ge	4.9×10^{19}	5.6×10^{19}	5×10^{19}	112	3.1829	5.1902
I	MOCVD	Ge	1.6×10^{20}	1.3×10^{20}	3.5×10^{20}	105	3.1844	5.1886

[14–18]. Furthermore we expand the investigated free electron concentration range to an upper limit of $n = 1.6\times10^{20}$ cm^{-3} including a detailed analysis of near band gap features of the imaginary part of the dielectric function. There we show the transition from Wannier-Mott to Mahan [20] excitons for increasing electron density both in absorption (ellipsometry) and emission (photoluminescence). Furthermore, we briefly discuss higher energy features in the dielectric functions of doped GaN with respect to a possible BGR effect and show that it is not observable up to a photon energy of 10 eV.

II. EXPERIMENT

For this study (0001) oriented wurtzite GaN samples with different electron densities were selected. When possible, bulk-like GaN crystals grown by hydride vapor phase epitaxy (HVPE) were used to reduce strain and decrease detrimental influences of buffer layers and foreign substrates on ellipsometric data analysis. However, for highest doping concentrations and thus free electron densities, heteroepitaxially grown GaN thin films were used.

The unintentionally doped (UID) sample A and the GaN:Si samples B–F were grown by HVPE in a vertical AIXTRON reactor on GaN seed layers deposited by metal organic vapor phase epitaxy (MOVPE) on c-plane sapphire substrates. Spontaneously separated large layer pieces with thickness of about 1 mm were cut into samples by wire-saw, afterwards double side-polished, and inductively coupled plasma (ICP) etched for subsequent optical characterization. More details are described in Ref. [21].

GaN:Ge samples G–I were grown by MOVPE in a single-wafer Aixtron AIX 200/4 RF-S reactor on sapphire substrates. An AlN/AlGaN seed and buffer layer was deposited on the sapphire before around 1.1 μm undoped GaN was grown. Finally, GaN:Ge was grown with a thickness of about 800 nm. More details about growth parameters can be found elsewhere [10]. These layers proved useful because of extremely smooth surfaces.

High-resolution x-ray diffraction was performed on all samples to determine lattice parameters. Measurement accuracies were ±0.0001 Å and ±0.0002 Å for the c and a lattice parameters, respectively. For unstrained GaN we adopted lattice parameters of $c_0 = 5.18523$ Å and $a_0 = 3.18926$ Å [22]. These values were used as reference to calculate the strain values for all analyzed samples. A summary of key parameters from all samples is presented in Table I. The lattice parameters and the strain values are visualized in Fig. 1. The strain values were used to correct for strain-induced band gap energy shifts. These shifts are $\Delta E_{\mathrm{strain}} < 2$ meV for samples A–F but reach values between 11 and 14 meV for samples G–I. Within the framework of the current study, the strain-dependent energy corrections are calculated as [23]

$$\Delta E_{\mathrm{strain}} = \varepsilon_{zz}(a_{\parallel} - D_1 - D_3) + 2\varepsilon_{xx}(a_{\perp} - D_2 - D_4), \qquad (1)$$

where $a_{\perp,\parallel}$ are the anisotropic deformation potentials of the conduction band, D_i ($i = 1,\ldots,4$) are deformation potentials of the valence bands, and ε_{zz} is the strain along the [0001] axis, while $\varepsilon_{xx} = \varepsilon_{yy}$ is the in-plane strain. Here, we use deformation potentials as determined by Ishii *et al.* [24], namely $a_{\parallel} - D_1 = -6.5$ eV, $a_{\perp} - D_2 = -11.2$ eV, $D_3 = 4.9$ eV, and $D_4 = -5.0$ eV. Resulting $\Delta E_{\mathrm{strain}}$ are summarized in Table II

The concentrations of Si and Ge for most of the samples were investigated by secondary ion mass spectroscopy (SIMS) with an uncertainty of 10%. The carrier density was measured both by Hall effect in van der Pauw geometry (uncertainty of 5%) and independently by infrared spectroscopic ellipsometry (IRSE) using a Woollam ellipsometer (300–6000 cm^{-1}). The dielectric function in the visible and ultraviolet spectral range

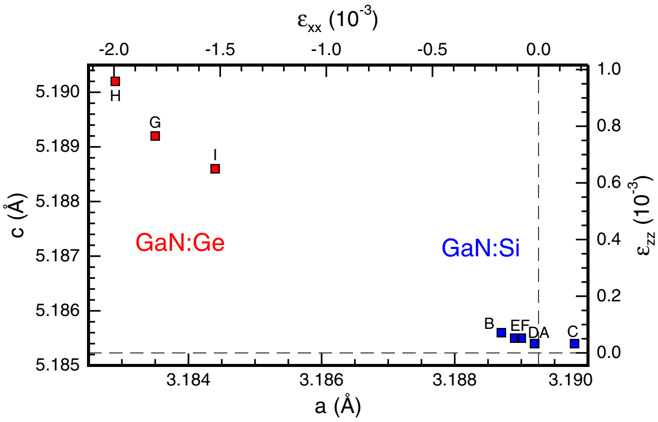

FIG. 1. (Color online) Experimentally obtained lattice parameters for the samples investigated. Hydride vapor phase epitaxy grown samples are marked blue, metal organic vapor phase epitaxy grown samples red. The strain values are given on the additional axes. All samples are labeled according to Table I.

TABLE II. Summary of characteristic energies E and energy shifts of the samples at room temperature. Characteristic energy values are exciton transition energies (samples A–F) or the onsets of the exciton continuum (samples G–I).

Sample	n_{Hall} (cm^{-3})	E (eV)	$\Delta E_{\mathrm{strain}}$ (meV)	ΔE_{BMS} (meV)	ΔE_{BGR} (meV)	$\Delta E_{\mathrm{Stokes}}$ (meV)
A	1.4×10^{12}	3.414	0	0	0	0
B	8.7×10^{17}	3.409	1	0	−45	7
C	1.8×10^{18}	3.406	−2	8	−56	3
D	3.3×10^{18}	3.427	0	20	−69	25
E	7.3×10^{18}	3.437	1	47	−91	32
F	1.4×10^{19}	3.470	0	83	−115	68
G	3.4×10^{19}	3.548	14	200	−153	98
H	4.9×10^{19}	3.592	14	254	−177	115
I	1.6×10^{20}	3.693	11	512	−286	

TABLE III. List of parameters for GaN as determined from sample A and taken from Ref. [27]. The static dielectric constants ε_{S} were determined by using the Lyddane-Sachs-Teller relationship.

	$\mathbf{E} \perp \mathbf{c}$	$\mathbf{E} \parallel \mathbf{c}$
m^*	$0.239m_0$	$0.216m_0$
ε_∞	5.16	5.30
ε_{S}	9.06	10.04
ω_{TO}	559.1 cm^{-1}	533.6 cm^{-1}
ω_{LO}	741.0 cm^{-1}	734.5 cm^{-1}

was obtained by sophisticated multilayer modeling [25] of variable angle spectroscopic ellipsometry data recorded by a Woollam VASE (0.5–6.5 eV). For ellipsometric data in the vacuum ultraviolet up to ≈10 eV samples B–I were analyzed by a dedicated VUV ellipsometer installed at the U125/2-NIM synchrotron beamline at the Berlin electron storage ring for synchrotron radiation (BESSY II). There, the angle of incidence was fixed to 67.5° [26]. All ellipsometric data were recorded at room temperature.

Finally, photoluminescence spectra were recorded at variable temperatures at two different setups. All samples were measured between 7 K and room temperature at different temperatures. The samples were mounted inside a helium-cooled cryostat and excited by the 325 nm line of a HeCd laser. The laser power of about 10 mW was focused on the sample yielding a circular spot size of about 1 mm (Fig. 10). Samples B–F were measured additionally at 10 K and at room temperature in a different setup where about 20 mW of HeCd laser power was focused down to a circular spot of around 40 μm in diameter (Fig. 11). The emitted light was detected by a grating monochromator with high focal length to which a liquid-nitrogen-cooled charge coupled device camera was mounted. The highest spectral resolution selected for this work was 180 μeV at 3.5 eV used for detecting the fine structure in the spectra of sample A at 7 K (Fig. 10).

III. RESULTS AND DISCUSSION

A. Infrared dielectric response

Infrared spectroscopic ellipsometry is sensitive to infrared active phonons. In our case phonons allowed for $\mathbf{E} \perp \mathbf{c}$ are observable of which the $E_1(TO)$ and the $E_1(LO)$ modes are of special interest. The latter one couples to plasmons stemming from the high free electron concentration, and yields a free carrier density dependent longitudinal phonon-plasmon coupled (LPP) mode split into two branches. The high energy branch, called LPP$_+$ is easily accessible in our spectral range and allows the determination of carrier concentrations for approximately $n > 10^{18}$ cm^{-3}. When neglecting damping, the energy position of the LPP$_+$ mode is given by

$$\omega_{\mathrm{LPP+}}^2 = \frac{\omega_{\mathrm{LO}}^2 + \omega_{\mathrm{P}}^2}{2} + \sqrt{\left(\frac{\omega_{\mathrm{LO}}^2 + \omega_{\mathrm{P}}^2}{2}\right)^2 - \omega_{\mathrm{TO}}^2\omega_{\mathrm{P}}^2}, \qquad (2)$$

using the squared plasma frequency

$$\omega_{\mathrm{P}}^2 = \frac{ne^2}{\varepsilon_\infty \varepsilon_0 m^*}. \qquad (3)$$

In Eqs. (2) and (3), ω_{LO} and ω_{TO} are the zero carrier density frequencies of the E_1 longitudinal (LO) and transversal optical (TO) phonon frequencies. These parameters were taken from our measurement results from sample A. n is the free electron concentration, e the elementary charge, ε_∞ is the high frequency limit of the dielectric constant, ε_0 the vacuum dielectric constant, and m^* the effective electron mass which is a constant input parameter here [27]. Parameters are tabulated in Table III.

Spectra were measured at different angles of incidence for every sample. Example results recorded at 60° and 72° are shown in Fig. 2 for the HVPE grown crystals. A detailed model of the ellipsometric parameters Ψ and Δ yields $\omega_{\mathrm{LPP+}}$ which can in turn be used to calculate ω_{P}. By Eq. (3) the free electron concentration is finally obtained. More details

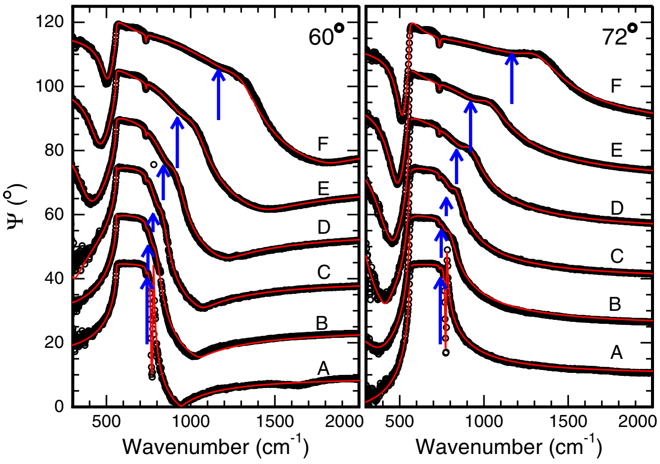

FIG. 2. (Color online) Infrared ellipsometry results (Ψ) for two selected angles of incidence (60° and 72°) and corresponding model fits for samples A–F. The symbols represent the experimental results, the red continuous lines the model fits. Resonance frequencies of the upper coupled phonon-plasmon mode (LPP$_+$) are marked by blue vertical arrows and yield the carrier densities n_{IRSE} in Table I.

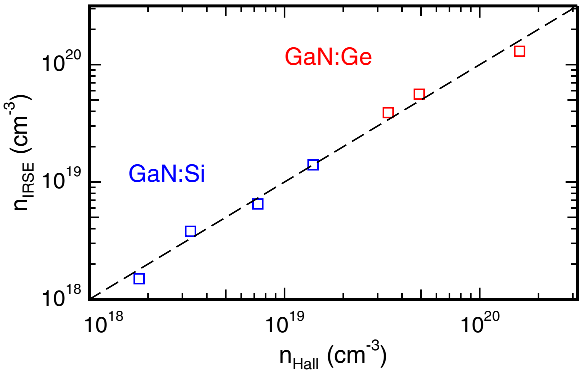

FIG. 3. (Color online) Carrier concentrations of samples C–I as obtained by infrared spectroscopic ellipsometry (IRSE) as a function of carrier concentrations determined by Hall effect measurements. The line represents equality. The effective electron mass is found to be constant at least up to a value of $n = 10^{20}$ cm^{-3}.

about the method can be found elsewhere [27]. Results are summarized in Table I as n_{IRSE}.

Free electron concentrations obtained by spectroscopic ellipsometry are compared to the values obtained by Hall effect measurements and agree very well (Fig. 3). This means the effective electron mass is constant within the doping range investigated here. For sample I a slight deviation from the linear behavior can be observed which is the beginning of conduction band nonparabolicity, similar to that discussed in earlier work [27]. The dopant atom concentration as determined by SIMS leads us to the conclusion that nearly all dopants are ionized at room temperature and the compensation ratio is low. Only for sample I with $n_{\mathrm{Hall}} = 1.6\times10^{20}$ cm^{-3} do we observe that less than half of the germanium atoms have released their electron into the conduction band. The same trend was observed earlier [10] and could be explained by self-compensation, gallium vacancy creation, or by placing dopant atoms not substitutionally on gallium sites but in clusters or complexes at the highest dopant concentrations, depending on the exact growth conditions [28].

B. Spectroscopic ellipsometry around the band edge

Absorption characteristics of the bulk-like GaN samples and the thin films were investigated by spectroscopic ellipsometry. From ellipsometric data the ordinary dielectric functions were extracted. Their imaginary parts ε_2 are shown in Fig. 4 around the absorption onset. For all samples, $\varepsilon_2 = 0$ below the absorption onset, while at around 4 eV the value of ε_2 is increasing from 1.6 for sample A up to 2 for sample I. The same effect was very recently found in theoretical calculations of heavily doped ZnO [29] and experimentally in highly Ge doped nonpolar $(11\bar{2}0)$ GaN [30]. It is thought to stem from intra-conduction-band transitions. An even more prominent feature is the energy shift of the absorption onset (steep increase in ε_2). This onset is found at higher energies for increasing electron concentration. Finally, the fine structure of the imaginary parts of the dielectric functions undergoes a remarkable change with increasing doping level. While sample A with the lowest free carrier concentration shows a strong excitonic resonance, visible as a sharp peak at the absorption onset, for increasing electron density all features broaden significantly. In samples G–I no different contributions can be distinguished anymore. The increasing broadening of these features as a function of electron density is due to the occupation of the conduction band and increasing disorder with higher doping levels.

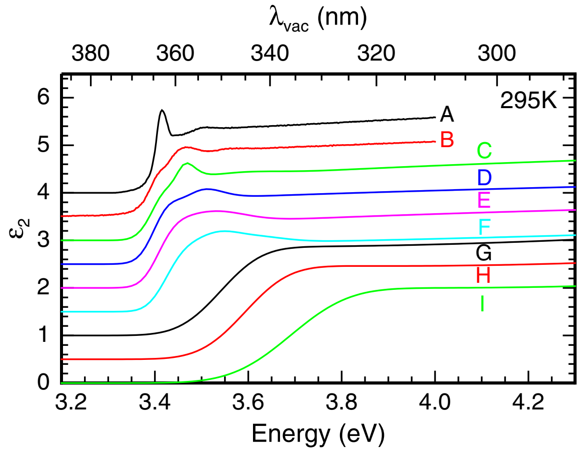

FIG. 4. (Color online) Imaginary parts of the ordinary dielectric functions of all samples around the band edge. The different spectra are vertically shifted by 0.5 for clarity.

A quantification of the discussed changes of the shape of ε_2 is done by line shape fitting of the different contributions adding to the imaginary part of the dielectric function. The fitting procedure is very similar to earlier published works in ZnMgO [31] and AlN [32] and contains basically Elliot's model [33] expanded for the treatment of exciton-phonon complexes [34]. To facilitate analysis we take into account only one exciton resonance representing free excitons with holes from both A and B valence bands and one weaker exciton resonance for the C exciton. All excitons are assumed to be broadened by Gaussian distributions; excited exciton states are neglected. However, the exciton continuum is of course taken into account. Finally, we allow for an exciton-phonon complex contribution which is included for samples A–C only. For electron concentrations higher than $n \approx 3\times10^{18}$ cm^{-3} the free carriers screen the exciton-phonon interaction effectively [35]. We use this analysis scheme for all presented samples even for those where the free carrier contribution is higher than the exciton Mott density which will be discussed below in detail. Indeed, for line shape analysis of ε_2 around the absorption onset we divide the excitonic contributions into Wannier-Mott and Mahan excitons below and above the exciton Mott density. The binding energy of Mahan excitons is set to zero while that of Wannier-Mott excitons is dependent on carrier density [see Eq. (11)]. Using luminescence data recorded at low temperatures we will refine this rough estimate to a more realistic continuous transition from the limiting cases of Wannier-Mott and Mahan excitons (Sec. IV).

Figure 5 presents results for the line shape analysis of ε_2 of samples A–F. All fitted line shapes show a close-to-perfect agreement with the measurement results. The resulting energy positions of the characteristic energies are discussed at the end of the following section. Note that the contribution from the C valence band (in analogy to cubic material frequently called split-off valence band) is increasing in relative intensity with

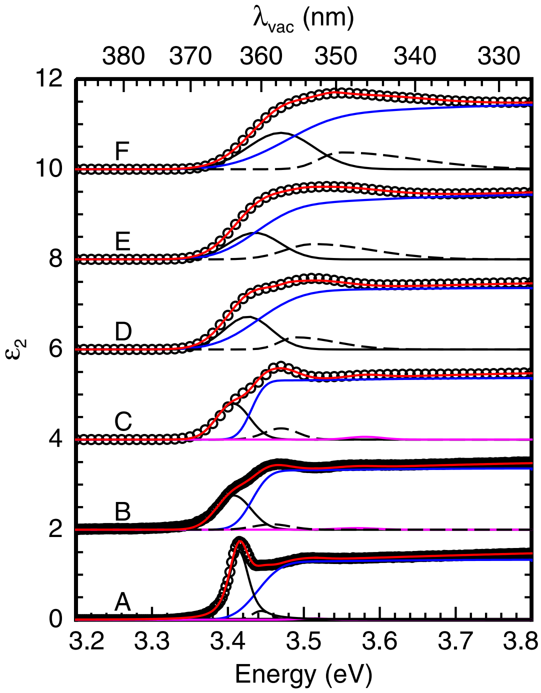

FIG. 5. (Color online) Line shape analysis of the imaginary parts of the dielectric functions from samples A–F in the region around the fundamental absorption edge. The spectra are shifted vertically by 2 for better visibility. Open circles represent the experimental ε_2, the lines are from the model. Black continuous lines represent Wannier-Mott or Mahan excitons with holes from the A and B valence bands, black dashed lines mean holes from the C valence band. Blue lines are the contributions from the exciton continuum, magenta are exciton-phonon complexes, and red is the sum of all contributions to the model.

increasing electron concentration. We want to stress that this is in agreement with **kp** theoretical calculations [34] when the wave vector k is increased.

C. Theoretical modeling

To describe the band gap renormalization (BGR) [3], we first have to define several basic terms. BGR is a lowering of the fundamental band gap energy of a semiconductor and is expected to be dominated by two contributions [4], namely electron-electron interaction (ΔE_{ee}) and electron ion interaction (ΔE_{ei}),

$$\Delta E_{\mathrm{BGR}} = \Delta E_{\mathrm{ee}} + \Delta E_{\mathrm{ei}}, \tag{4}$$

with ΔE_{BGR} the overall change of the band gap energy. Both ΔE_{ee} and ΔE_{ie} can be approximated analytically. The electron-electron interaction is given by

$$\Delta E_{\mathrm{ee}} = -\frac{e^2 k_{\mathrm{F}}}{2\pi^2 \varepsilon_0 \varepsilon_{\mathrm{S}}} - \frac{e^2 k_{\mathrm{TF}}}{8\pi \varepsilon_0 \varepsilon_{\mathrm{S}}}\left[1 - \frac{4}{\pi}\arctan\left(\frac{k_{\mathrm{F}}}{k_{\mathrm{TF}}}\right)\right], \tag{5}$$

while electron-ion interaction is approximated by

$$\Delta E_{\mathrm{ei}} = -\frac{e^2 n}{\varepsilon_0 \varepsilon_{\mathrm{S}} a^*_{\mathrm{B}^-} k^3_{\mathrm{TF}}}. \tag{6}$$

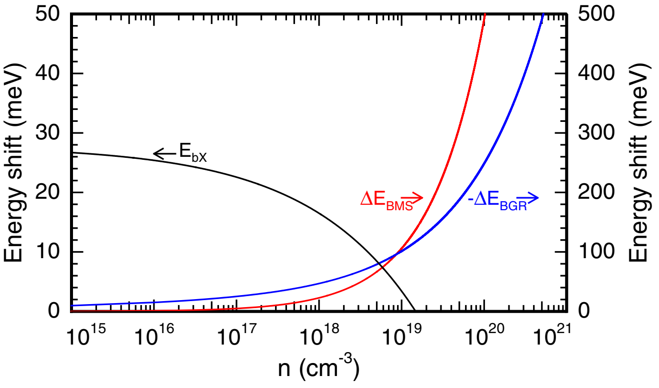

FIG. 6. (Color online) (Black) Exciton binding energy E_{bX} as a function of electron concentration. The exciton Mott transition is approximated as the point, where $E_{\mathrm{bX}} = 0$. (Red) Burstein-Moss shift ΔE_{BMS} and (blue) band-gap renormalization $-\Delta E_{\mathrm{BGR}}$ due to increasing free electron density. It can be clearly seen that, at around 9×10^{18} cm^{-3}, the effect of BMS overcomes that of BGR.

The abbreviations in Eqs. (5) and (6) are the Fermi vector $k_{\mathrm{F}} = (3\pi n)^{1/3}$ and the estimated inverse Thomas-Fermi screening length $k_{\mathrm{TF}} = 2\sqrt{k_{\mathrm{F}}/(\pi a^*_{\mathrm{B}^-})}$. We neglect crystal anisotropy here, introducing a small error in our calculations, since an exact treatment would require numerical methods which we want to avoid. The screened Bohr radius also known as effective Bohr radius of the electron is

$$a^*_{\mathrm{B}^-} = \frac{4\pi \varepsilon_0 \varepsilon_{\mathrm{S}} \hbar^2}{m^*_{\mathrm{De}} e^2} = 2.15 \text{ nm}. \tag{7}$$

ε_{S} is the static dielectric constant of GaN. We use the weigthed geometric mean value of

$$\varepsilon_{\mathrm{S}} = \sqrt[3]{\varepsilon^2_{\mathrm{S}\perp} \varepsilon_{\mathrm{S}\parallel}} = 9.38, \tag{8}$$

m^*_{De} is the density-of-states mass which has to be used instead of the electron effective mass m^*_{e} due to the degenerate electron concentrations populating the entire three-dimensional density of states. We obtain

$$m^*_{\mathrm{De}} = (m^*_{\mathrm{e},\parallel} m^{*}_{\mathrm{e},\perp}{}^2)^{1/3} = 0.231 m_0 \tag{9}$$

for electron effective masses as given in Table III. The calculated downward shift of the fundamental band gap of GaN with increasing electron concentration is demonstrated in Fig. 6 as $-\Delta E_{\mathrm{BGR}}$.

The Burstein-Moss shift is an upward shift of the absorption edge of highly doped material. The idea of BMS is successive population of band-states by carriers which relax to the lowest available energy. Due to Pauli-blocking this energy increases with increasing carrier density, making a semiconductor transparent up to the degenerate Fermi energy level. BMS in the conduction band follows the law

$$\Delta E_{\mathrm{BMS}} = \frac{\hbar^2 k^2_{\mathrm{F}}}{2 m^*_{\mathrm{De}}}. \tag{10}$$

Because optical absorption of a photon is a direct momentum conserving transition (neglecting the momentum of the photon) also the valence band energy at k_{F} has to be considered. The polarization direction of the electric field vector is mainly

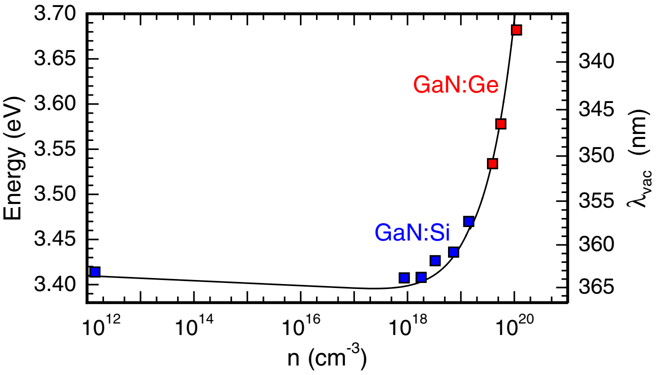

FIG. 7. (Color online) Transition energy values of the Wannier-Mott or Mahan exciton of the samples as a function of free electron concentration as determined by Hall effect measurements (symbols). The shown data points are already shifted to correct for strain. The continuous line demonstrates $E(n)$ resulting from our model calculations as described in the text and in Eq. (12). This is the sum of the three contributions shown in Fig. 6.

perpendicular to [0001] in all cases investigated here, i.e., $\mathbf{E} \perp \mathbf{c}$, thus for the valence band dispersion only the effective hole mass for $\mathbf{E} \perp \mathbf{c}$ has to be used. To obtain the absorption onset, we only have to take into account the mass of the valence band with the highest energy, which is $m^*_{\mathrm{h},\perp} = 0.57m_0$ [36]. The simplest way to include this effect is to use a reduced effective mass $\mu^*_{\mathrm{BMS}} = (m^*_{\mathrm{De}} m^*_{\mathrm{h},\perp})/(m^*_{\mathrm{De}} + m^*_{\mathrm{h},\perp}) = 0.16m_0$ replacing m^*_{De} in Eq. (10). The reduced effective mass accounts for both masses of electron and hole and therefore already contains the curvatures of conduction and valence bands which both contribute to the blue shift of the absorption onset. In Fig. 6 the overall dependence of ΔE_{BMS} for $\mathbf{E} \perp \mathbf{c}$ is shown including the contribution arising from the valence band.

A third very important effect when considering the energy of the absorption onset especially at lower carrier densities is the Wannier-Mott exciton binding energy which is also dependent on the free carrier density. A high density of charge carriers screens the Coulomb interaction between electrons and holes successively. A possible criterion to define the Mott density is thus to use the electron density when the exciton binding energy is approaching zero. This value is then called the exciton Mott density. The reduction of the free exciton binding energy can be estimated by the exchange energy. For our case the absolute value of the Wannier-Mott exciton binding energy is therefore

$$E_{\mathrm{bX}} = \frac{e^2}{8\pi\varepsilon_0\varepsilon_S a^*_{\mathrm{B^x}}} - \frac{3e^2(3\pi^2)^{1/3}}{(4\pi)^2\varepsilon_0\varepsilon_S} n^{1/3}. \qquad (11)$$

However, the effective electron mass entering $a^*_{\mathrm{B^x}}$ in Eq. (11) is the reduced effective mass, this time averaged over the three-dimensional density of states both in the conduction and in the valence bands. For the highest valence band m^*_{Dh} equals $0.87m_0$ [36], the reduced effective mass is $\mu^* = (m^*_{\mathrm{De}} m^*_{\mathrm{Dh}})/(m^*_{\mathrm{De}} + m^*_{\mathrm{Dh}}) = 0.18m_0$, the screened exciton Bohr radius amounts to $a^*_{\mathrm{B^x}} = 2.76$ nm, and the calculated zero density exciton binding energy, defined by the first term in Eq. (11), is 28 meV, in excellent agreement with more sophisticated calculations [37]. The exciton Mott density according to this definition is $n_{\mathrm{Mott}} = 1.5\times10^{19}$ cm^{-3}. The functional dependence of E_{bX} on the charge carrier density is shown as well in Fig. 6.

Instead of the concept of an exciton Mott transition, a continuous transition between Wannier-Mott excitons below and Mahan excitons [38] above the exciton Mott density would be more appropriate [39]. For the line shape fits of room temperature ε_2 data (Fig. 5), it is sufficient to set the Mahan exciton binding energy to zero. This holds because measured energy shifts are dominated by other effects especially BMS and BGR for higher carrier concentrations and by Wannier-Mott exciton screening at lower carrier densities. Note, that the exciton binding energy roughly follows an exponential decrease for increasing free carrier density as shown for ZnO in Ref. [39]; however, no closed analytical expression seems to be available yet.

From line shape analysis of the imaginary part of the dielectric functions we obtained exciton transition energies. These values were corrected for the measured strain values of each sample as explained before (values are given in Table II), and are shown in Fig. 7. The theoretical calculated exciton energy is also shown as continuous line using

$$E(n) = E_{\mathrm{gap}} - E_{\mathrm{bX}} + \Delta E_{\mathrm{BGR}} + \Delta E_{\mathrm{BMS}} \qquad (12)$$

with $E_{\mathrm{gap}} = 3.437$ eV [40]. The exciton binding energy term is only included up to n_{Mott} according to Eq. (11). The overall agreement of the model with the experimentally found energy values is excellent, confirming on the one hand the accuracy of the line shape analysis and on the other hand the quality of even the highly doped samples. Explicit values for ΔE_{BGR} and ΔE_{BMS} of all samples are summarized in Table II.

Finally, the current data provides insight in a further subject of absorption features around the band edge, namely transitions from the C valence band to the conduction band at the Fermi wave vector (Fig. 5). In a simplified picture, the exciton consisting of an electron and a hole from the C valence band will be screened in the same way as an A or B exciton. Therefore, the distance between the C valence band related absorption to the A/B valence band one yields an estimate for the valence subband splitting. A detailed analysis can be performed for samples A–F only as the spectra from heteroepitaxially grown samples G–I do not allow definite deconvolution into different contributions. These results as a function of the estimated Fermi wave vector k_{F} are presented in Fig. 8. For comparison we show as well two quadratic valence bands according to $E(k) = -\hbar^2k^2/(2m^*_h)$ with constant effective hole masses representing the A/B valence bands and the separated C valence band. The effective masses used are $m^*_{\mathrm{A/B,h}} = 0.92m_0$ and $m^*_{\mathrm{C,h}} = 0.31m_0$ [36] neglecting additional fine structure, crossings, anticrossings, and so on. Besides these simplifications we find a nice agreement, allowing the conclusion that we do in fact observe C valence band related absorption here and that the effective hole mass $m^*_{\mathrm{C,h}}$ is indeed close to $0.31m_0$ as predicted [36].

D. High energy features

Recently, it was discussed whether band gap renormalization also occurs in higher energy conduction bands or if the effect is limited to the lowest conduction band only [29].

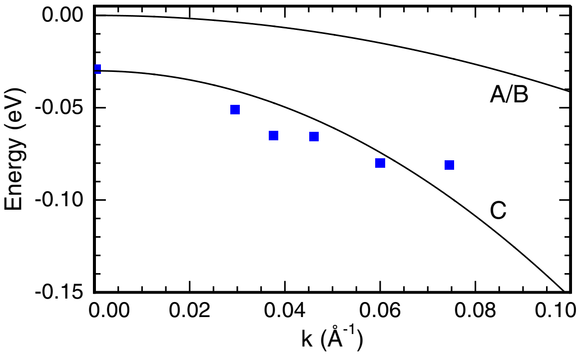

FIG. 8. (Color online) Valence band structure of GaN from the Γ point in the direction of the M or K point. Symbols represent measured energy differences between absorption from A/B and C valence band related features, continuous lines stand for a simplified quadratic valence band structure with constant effective hole masses.

To make a step forward to clarify this issue experimentally, we have measured spectroscopic ellipsometry up to 9.7 eV. Results for samples B–I are presented in Fig. 9. It is obvious that the high energy contributions do not shift markedly. Only for the heteroepitaxially grown samples G–I is a small but constant shift to lower energies observable, which is apparently related to the different set of samples rather than to BGR. The changed intensity ratio of the high energy features could be linked to different roughness. A BGR shift of the order of 115 meV for sample F or even 286 meV for sample I (see Table II) would be easily detectable in our experiment. This means, BGR does not cause a rigid shift of all conduction bands towards lower energies leading to decreased transition energies.

The prominent high energy features falling within our spectral range are labeled $E_1(B)$ (at around 7 eV), $E_1(C)$ (at 7.9 eV), and E_2 (at 9.2 eV) according to Ref. [26]. They are identified with interband transitions far from the center of the Brillouin zone, namely between M and L point [$E_1(B)$], at the M point [$E_1(C)$], and at the K point (E_2). The next transition occurring at the Γ point; i.e., at $k = 0$, would be E_0' expected at around 13 eV, which is beyond the spectral range of this study. The possibility that E_0' exhibits renormalization effects remains unresolved here.

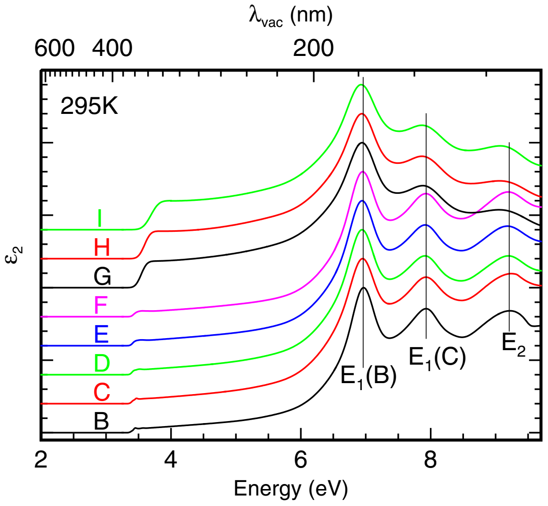

FIG. 9. (Color online) Imaginary parts of the ordinary dielectric functions of samples B–I in the energy region up to 9.7 eV. The spectra are normalized to the amplitude of $E_1(B)$ and shifted vertically for clarity to facilitate the comparison of energy positions.

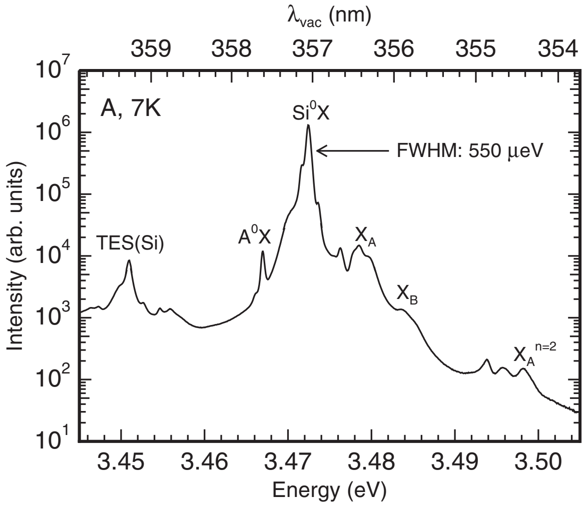

FIG. 10. High resolution excitonic photoluminescence spectrum of sample A at $T = 7$ K.

IV. PHOTOLUMINESCENCE

A. Sample A

The unintentionally doped GaN sample A shows the expected very sharp and intense photoluminescence features. The spectrum shown in Fig. 10 presents a dominant shallow neutral donor bound exciton at 3.4723 eV. The corresponding two-electron satellite (TES) at 3.4508 eV identifies this donor as silicon-on-gallium site. At our temperature $T = 7$ K the dominant TES transition is the one related to the $2p_0$ state of the donor, the distance between Si^0X and the TES peak of 21.5 meV then yields a one-particle donor binding energy of $E_{\mathrm{D,Si}} = 29.3$ meV by the formalism presented by Paskov and coworkers [41]. Note that the small low energy shoulder of the donor bound exciton can be identified by the shallow donor bound exciton at the oxygen-on-nitrogen site, yielding $E_{\mathrm{D,O}} = 32.3$ meV by comparing its TES energy position at 3.4472 eV. The strength of the silicon related line in comparison to the one related to oxygen may be explained by the intentional use of silicon as a dopant in this HVPE reactor, and an oxygen background below 2×10^{16} cm^{-3} [21].

The energy position of Si^0X in our sample is 1.4 meV higher than that of the donor bound exciton reported in Ref. [42] while our acceptor bound exciton is located at 3.4668 eV which is 2.5 meV higher than in Ref. [42]. The distance between Si^0X and O^0X is around 800 μeV [43]. However, it was mentioned that the GaN layer grown by MOVPE on a bulk GaN sample in Ref. [42] showed a tensile in-plane strain of about 3×10^{-4}, which corresponds roughly to this energy shift of 2.5 meV. In this case, we can identify the donor bound exciton in Ref. [42] as O^0X.

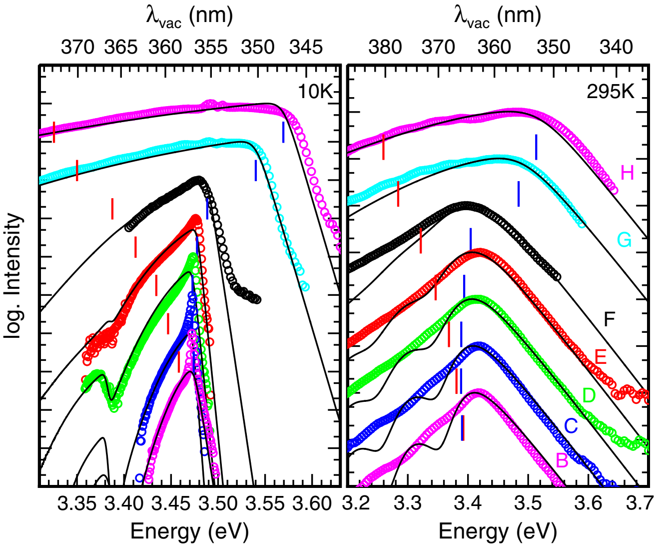

FIG. 11. (Color online) Photoluminescence spectra of samples B–H (from bottom to top) at low temperature (left) and at room temperature (right). Experimental spectra are plotted by open symbols, a model luminescence line shape taking into account free carrier emission (i.e., band-to-band emission and phonon replica) is shown as continuous lines. All spectra are offset vertically for clarity. The energy positions of $E_{\text{gap}} + \Delta E_{\text{BGR}}$ and $E_{\text{gap}} + \Delta E_{\text{BGR}} + \Delta E_{\text{BMS}}$ are marked by red and blue short vertical lines, respectively.

B. Intentionally doped samples B–H

The photoluminescence spectra of the doped samples (Fig. 11) undergo characteristic changes with increasing electron density mirroring BGR and BMS. At first, the sharp features related to the excitonic recombinations disappear at $T = 10$ K, and the photoluminescence starts to broaden at the low energy wing. The energy of the intensity maximum remains almost constant up to $n = 7.3\times10^{18}$ cm^{-3} (sample E). Continuously increasing broadening starts to develop for higher carrier densities as seen for samples F (GaN:Si) and G and H (GaN:Ge). The tiny features on top of the 10 K spectra from samples G and H at around 3.49 eV and 3.50 eV stem from buried undoped but heavily strained GaN buffer layers. They are most likely excited by the PL signal of the doped top layer which is in turn transparent for the lower energy bands from the buried film. This assignment is further evidenced by HRXRD results yielding also lattice parameters of the buffer layers, and independently by measured exciton energies of bare buffer layers. The film with the highest doping level (I) did not show luminescence from the doped layer by excitation with HeCd laser light and is therefore omitted here. The general PL line shape can be approximated satisfactorily by textbook models where electrons in the conduction band recombine with holes localized at the valence band maximum as described earlier for highly doped GaN [44]. As the high doping concentrations needed for the corresponding free electron densities create band tails in the band gap, these band tails must be taken into account as well.

The high energy wing of the PL signal in all samples is found approximately at the position of the Fermi energy measured from the valence band maximum, unlike in ellipsometry, where the valence band dispersion up to the Fermi vector also adds up to the absorption onset. This means the photoluminescence process in our highly doped GaN samples does not fulfill $\Delta k = 0$, thus most probably a remarkable valence band tailing must occur to mediate between k_{F} in the conduction band and the Γ point in the valence band. The slope of this high energy wing is governed by the Fermi-Dirac distribution. At very low temperatures, the carrier temperature for modeling had to be increased by some ten Kelvin to achieve sufficient agreement, similar to earlier studies [13,44]. The position of the Fermi energy represented by $E_{\text{gap}} + \Delta E_{\text{BGR}} + \Delta E_{\text{BMS}}$ measured from the valence band maximum, and of the renormalized band gap given by $E_{\text{gap}} + \Delta E_{\text{BGR}}$, are marked by vertical lines in Fig. 11; ΔE_{BGR}, ΔE_{BMS}, and the carrier densities are assumed to be independent of temperature.

The modeled luminescence line shapes shown in Fig. 11 consist basically of a Kane density of states for the conduction band [45] multiplied by the Fermi-Dirac distribution accounting for the population probability, very similar to the approach described in Ref. [44]. For calculating the line shapes, only the renormalized band gap energy, the Fermi energy, and a characteristic parameter G describing the band tailing are needed. Here, we do not calculate G from the impurity potential fluctuations but we derive G from fitting to the PL line shapes. Finally, longitudinal optical phonon replica are added. While the energies are already known from the calculations above (verified by the excellent agreement with ellipsometry results), G is the only fitting parameter. We summarize resulting values for G in Fig. 12. Note that the values for samples B–F are similar to the values found in Ref. [44] for a parabolic conduction band (compare with Fig. 3 there). However, our values for the thin films are larger, possibly due to further sources of local potential fluctuations introduced by heteroepitaxy. Comparing the line shape models to the measured PL spectra, we find an overall good agreement with certain inaccuracies especially at the low energy wings. However, it is well known that the Kane density of states overestimates the number of states in the band tail [46], and,

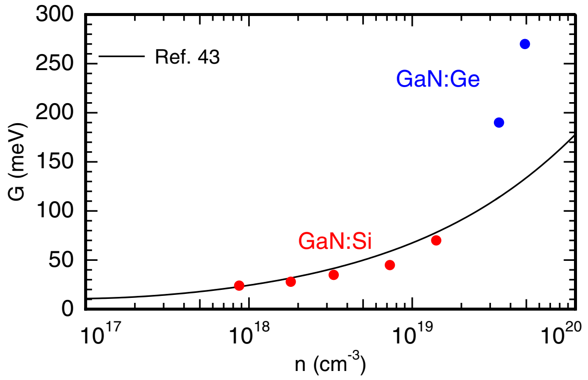

FIG. 12. (Color online) Band tailing parameter G as a function of free carrier concentration as obtained from model fits of the photoluminescence line shape to the measured spectra (symbols) in comparison to calculated results for a parabolic conduction band from Ref. [44] (continuous curve).

on the other hand, our empirical estimate for G is expected to introduce a certain error as well. Nevertheless, the main features of luminescence are well reproduced by our approach. A more detailed analysis of the band tail line shape is beyond the scope of this study.

In samples B–E one can see a luminescence peak (in 10 K spectra) approximately at the position of the Fermi energy which is not reproduced by the model. It is stronger in intensity for lower doped samples. Temperature dependent luminescence studies show that these peaks merge with the broad band-to-band recombination at elevated temperatures (≈80 K). These contributions cannot be identified by donor bound or classical Wannier-Mott free excitons due to their energy position at the Fermi energy and not below the renormalized band gap energy. Therefore, these bands are identified as Mahan excitons, as found earlier for different material systems in luminescence [38,47]. To be more accurate, these exciton resonances are identified with free excitons whose binding energy is partially screened by free carriers.

From the peak energy of these excitons (visible clearly in samples B–E) and the position of the corresponding calculated Fermi energies, the exciton binding energies are extracted. The values for the exciton binding energies are all below 2 meV, namely 1.9 meV (sample B), 0.3 meV (C), 1.0 meV (D), and 1.8 meV (E). We note that our estimate for the screened Wannier-Mott exciton binding energy [Eq. (11)] yields larger values in the range from 8 to 18 meV for the given electron densities. However, we expect the real dependence of the exciton binding energy on free carrier density to be a continuous transition from Wannier-Mott to Mahan excitons [39]. A more refined theory might yield better agreement to experiment. Furthermore, to extract the exciton binding energy we used the calculated position of the Fermi energy, whose accuracy might be an issue.

For the line shape fits to ε_2 (Fig. 5) we have set the Mahan exciton binding energy to zero and the room temperature Wannier-Mott exciton binding energy according to Eq. (11), which is completely justified by the low experimental values of Mahan exciton binding energies. Nevertheless, more research on this subject is needed.

We find that neither PL peak position nor its FWHM can be used to directly estimate the doping concentration in GaN. The same holds for the so-called Stokes shift. The Stokes shift is defined by the energetic separation of the Wannier-Mott or Mahan exciton as determined from the dielectric function and the intensity maximum of the PL band at the same temperature. It increases from zero (sample A) up to 68 meV (sample F) for the GaN:Si HVPE crystals. The GaN:Ge films reach even higher values. Detailed results are given in Table II. Therefore, it is not possible to accurately determine doping concentrations alone from simple spectroscopic features of photoluminescence spectra, such as FWHM or Stokes shift.

V. SUMMARY

The influence of high electron densities on the absorption and emission characteristics of wurtzite GaN was investigated in detail. The absorption properties were represented by imaginary parts of the ordinary dielectric functions obtained from spectroscopic ellipsometry data. Line shape fits to these dielectric functions were performed to model the carrier dependent absorption behavior around the band gap. Discrete exciton transitions around the Γ point of the Brillouin zone dominate in the low electron density regime. For slightly larger n, exciton screening is observed. At very high carrier concentrations, the absorption edge is shifted from the Γ point of the Brillouin zone to the Fermi wave vector. The data are quantitatively discussed in terms of exciton screening, band gap renormalization (ΔE_{BGR}), and Burstein-Moss shift (ΔE_{BMS}). Renormalization and Burstein-Moss effect nearly cancel each other out for low free electron concentrations. The Burstein-Moss effect exceeds the gap shrinkage for $n \geqslant 9\times10^{18}$ cm^{-3} yielding a net blue shift of the absorption onset. The sample with the highest free carrier concentration ($n_{\mathrm{Hall}} = 1.6 \times 10^{20}$ cm^{-3}) yields $\Delta E_{\mathrm{BGR}} = -286$ meV and $\Delta E_{\mathrm{BMS}} = 512$ meV. In contrast, transitions related to high energy critical points of the band structure do not show renormalization effects. Moreover, we determined the effective mass of the C valence band by observation of direct transitions at the Fermi wave vector from the C valence band to the Fermi energy. Photoluminescence spectra from highly doped samples show recombination from the filled conduction band to the valence band maximum at the Γ point. The Fermi energy is visible in the spectra as steep decrease at the high energy of the emission bands while the renormalized band gap energy determines the low energy onset of emission. Additionally, band tail states have to be considered to quantitatively describe photoluminescence spectra. Close to the Fermi energy the Mahan exciton recombination was identified at low temperatures, yielding an estimate for the screened exciton binding energy.

ACKNOWLEDGMENTS

We gratefully acknowledge support by the synchrotron radiation sources BESSY II of the Helmholtz-Zentrum Berlin (HZB), Germany, by the Deutsche Forschungsgemeinschaft DFG in the framework of the Major Research Instrumentation Program under Projects No. INST 272/205-1 and No. INST 272/211-1 and the Collaborative Research Center 787, and by the Federal Ministry of Education and Research under Projects No. 16BM1202 (TeleGaN) and No. 13N10253 (GaNonSi).

---

[1] T. S. Moss, Proc. Phys. Soc. B **67**, 775 (1954).
[2] E. Burstein, Phys. Rev. **93**, 632 (1954).
[3] K.-F. Berggren and B. E. Sernelius, Phys. Rev. B **24**, 1971 (1981).
[4] R. A. Abram, G. J. Rees, and B. L. H. Wilson, Adv. Phys. **27**, 799 (1978).
[5] G. D. Mahan, J. Appl. Phys. **51**, 2634 (1980).

[6] H. Teisseyre, P. Perlin, T. Suski, I. Grzegory, S. Porowski, J. Jun, A. Pietraszko, and T. D. Moustakas, J. Appl. Phys. **76**, 2429 (1994).

[7] P. Prystawko, M. Leszczynski, B. Beaumont, P. Gibart, E. Frayssinet, W. Knap, P. Wisniewski, M. Bockowski, T. Suski, and S. Porowski, Phys. Status Solidi B **210**, 437 (1998).

[8] S. N. Svitasheva and A. M. Gilinsky, Appl. Surf. Sci. **281**, 109 (2013).

[9] R. Kirste, M. P. Hoffmann, E. Sachet, M. Bobea, Z. Bryan, I. Bryan, C. Nenstiel, A. Hoffmann, J.-P. Maria, R. Collazo, and Z. Sitar, Appl. Phys. Lett. **103**, 242107 (2013).

[10] S. Fritze, A. Dadgar, H. Witte, M. Bügler, A. Rohrbeck, J. Bläsing, A. Hoffmann, and A. Krost, Appl. Phys. Lett. **100**, 122104 (2012).

[11] D. C. Reynolds, D. C. Look, and B. Jogai, J. Appl. Phys. **88**, 5760 (2000).

[12] T. Nagai, T. J. Inagaki, and Y. Kanemitsu, Appl. Phys. Lett. **84**, 1284 (2004).

[13] F. Binet, J. Y. Duboz, J. Off, and F. Scholz, Phys. Rev. B **60**, 4715 (1999).

[14] M. Yoshikawa, M. Kunzer, J. Wagner, H. Obloh, P. Schlotter, R. Schmidt, N. Herres, and U. Kaufmann, J. Appl. Phys. **86**, 4400 (1999).

[15] I.-H. Lee, J. J. Lee, P. Kung, F. J. Sanchez, and M. Razeghi, Appl. Phys. Lett. **74**, 102 (1999).

[16] Z. Chine, A. Rebey, H. Touati, E. Goovaerts, M. Oueslati, B. El Jani, and S. Laugt, Phys. Status Solidi A **203**, 1954 (2006).

[17] H. P. D. Schenk, S. I. Borenstain, A. Berezin, A. Schön, E. Cheifetz, S. Khatsevich, and D. H. Rich, J. Appl. Phys. **103**, 103502 (2008).

[18] S. Shokhovets, K. Köhler, O. Ambacher, and G. Gobsch, Phys. Rev. B **79**, 045201 (2009).

[19] R. Dwiliński, R. Doradziński, J. Garczyński, L. P. Sierzputowski, A. Puchalski, Y. Kanbara, K. Yagi, H. Minakuchi, and H. Hayashi, J. Cryst. Growth **311**, 3015 (2009).

[20] G. D. Mahan, Phys. Rev. **153**, 882 (1967).

[21] E. Richter, T. Stoica, U. Zeimer, C. Netzel, M. Weyers, and G. Tränkle, J. Electron. Mater. **42**, 820 (2013).

[22] V. Darakchieva, B. Monemar, and A. Usui, Appl. Phys. Lett. **91**, 031911 (2007).

[23] G. Rossbach, M. Feneberg, M. Röppischer, C. Werner, N. Esser, C. Cobet, T. Meisch, K. Thonke, A. Dadgar, J. Bläsing, A. Krost, and R. Goldhahn, Phys. Rev. B **83**, 195202 (2011).

[24] R. Ishii, A. Kaneta, M. Funato, Y. Kawakami, and A. A. Yamaguchi, Phys. Rev. B **81**, 155202 (2010).

[25] R. Goldhahn, Acta Phys. Pol. A **104**, 123 (2003).

[26] C. Cobet, R. Goldhahn, W. Richter, and N. Esser, Phys. Status Solidi B **246**, 1440 (2009).

[27] M. Feneberg, K. Lange, C. Lidig, M. Wieneke, H. Witte, J. Bläsing, A. Dadgar, A. Krost, and R. Goldhahn, Appl. Phys. Lett. **103**, 232104 (2013).

[28] P. Bogusławski and J. Bernholc, Phys. Rev. B **56**, 9496 (1997).

[29] J. Jung and T. G. Pedersen, J. Appl. Phys. **113**, 114904 (2013).

[30] M. Wieneke, H. Witte, K. Lange, M. Feneberg, A. Dadgar, J. Bläsing, R. Goldhahn, and A. Krost, Appl. Phys. Lett. **103**, 012103 (2013).

[31] M. D. Neumann, C. Cobet, N. Esser, T. A. Wassner, B. Laumer, M. Eickhoff, M. Feneberg, and R. Goldhahn, J. Appl. Phys. **110**, 013520 (2011).

[32] M. Feneberg, M. F. Romero, M. Röppischer, C. Cobet, N. Esser, B. Neuschl, K. Thonke, M. Bickermann, and R. Goldhahn, Phys. Rev. B **87**, 235209 (2013).

[33] R. J. Elliot, Phys. Rev. **108**, 1384 (1957).

[34] S. Shokhovets, O. Ambacher, B. K. Meyer, and G. Gobsch, Phys. Rev. B **78**, 035207 (2008).

[35] M. S. Skolnick, K. J. Nash, P. R. Tapster, D. J. Mowbray, S. J. Bass, and A. D. Pitt, Phys. Rev. B **35**, 5925 (1987).

[36] L. C. de Carvalho, A. Schleife, and F. Bechstedt, Phys. Rev. B **84**, 195105 (2011).

[37] A. V. Rodina, M. Dietrich, A. Göldner, L. Eckey, A. Hoffmann, Al. L. Efros, M. Rosen, and B. K. Meyer, Phys. Rev. B **64**, 115204 (2001).

[38] M. Feneberg, J. Däubler, K. Thonke, R. Sauer, P. Schley, and R. Goldhahn, Phys. Rev. B **77**, 245207 (2008).

[39] A. Schleife, C. Rödl, F. Fuchs, K. Hannewald, and F. Bechstedt, Phys. Rev. Lett. **107**, 236405 (2011).

[40] B. Monemar, P. P. Paskov, J. P. Bergman, A. A. Toropov, T. V. Shubina, T. Malinauskas, and A. Usui, Phys. Status Solidi B **245**, 1723 (2008).

[41] P. P. Paskov, Talk at the International Workshop on Nitride Semiconductors, Tampa, 2010 (unpublished).

[42] K. Kornitzer, T. Ebner, K. Thonke, R. Sauer, C. Kirchner, V. Schwegler, M. Kamp, M. Leszczynski, I. Grzegory, and S. Porowski, Phys. Rev. B **60**, 1471 (1999).

[43] W. J. Moore, J. A. Freitas Jr., G. C. B. Braga, R. J. Molnar, S. K. Lee, K. Y. Lee, and I. J. Song, Appl. Phys. Lett. **79**, 2570 (2001).

[44] B. Arnaudov, T. Paskova, E. M. Goldys, S. Evtimova, and B. Monemar, Phys. Rev. B **64**, 045213 (2001).

[45] E. O. Kane, Phys. Rev. **131**, 79 (1963).

[46] P. Van Mieghem, Rev. Mod. Phys. **64**, 755 (1992).

[47] F. Fuchs, K. Kheng, P. Koidl, and K. Schwarz, Phys. Rev. B **48**, 7884 (1993).